

Ultracompact Photonic Circuits without Cladding Layers

Tongtong Song^{1,§}, Hongchen Chu^{1,§}, Jie Luo^{2,§}, Zizheng Cao,³ Meng Xiao,⁴
Ruwen Peng^{1,*}, Mu Wang^{1,5,†}, and Yun Lai^{1,‡}


¹National Laboratory of Solid State Microstructures, School of Physics, and Collaborative Innovation Center of Advanced Microstructures, Nanjing University, Nanjing, 210093, China

²School of Physical Science and Technology, Soochow University, Suzhou, 215006, China

³Institute for Photonic Integration, Eindhoven University of Technology,
P.O. Box 5135600 MB Eindhoven, Netherlands

⁴Key Laboratory of Artificial Micro- and Nano-structures of Ministry of Education and School of Physics and Technology, Wuhan University, Wuhan, 430072, China

⁵American Physical Society, 1 Research Road, Ridge, New York 11961, USA

 (Received 26 June 2021; revised 3 January 2022; accepted 8 February 2022; published 21 March 2022)

Cladding layers of waveguides prevent interchannel interference yet are unfavorable for the integration of photonic circuits. Here, we report the realization of ultracompact waveguide arrays, bends, and circuits with essentially zero interchannel separation. This supercompactness is achieved via arrays of waveguides with shifted spatial dispersions, where each waveguide functions as both the transmission channel and an effective “cladding layer” of its neighboring waveguides, and has been experimentally realized in low-loss all-dielectric photonic crystals. We show that the zero-spacing transmission array possesses the remarkable features of negligible crosstalk, high-efficiency sharp bending, and ultracompact photonic routing where the light can traverse the entire physical space. This finding opens a new avenue for extreme space utilization efficiency in waveguide physics and integrated photonics.

DOI: [10.1103/PhysRevX.12.011053](https://doi.org/10.1103/PhysRevX.12.011053)

Subject Areas: Metamaterials, Optics, Photonics

I. INTRODUCTION

In the pursuit of highly compact optical waveguides, photonic integrated circuits [1–7] move from the low-refractive-index-contrast material systems (e.g., SiO₂ on Si) to the high-contrast ones [e.g., silicon-on-insulator (SOI)], where the cross-sectional areas of waveguides are reduced by more than 2 orders of magnitude. Recently, great endeavors have been made to further increase the integration density by using plasmonic waveguides [8–10] or ultrahigh-refractive-index-contrast optical waveguides [11,12]. However, the cladding layers still impose a fundamental challenge on the interchannel separation and overall compactness. The cladding or

wave-forbidden layers are generally considered indispensable in general waveguide systems [13] such as optical fibers, photonic integrated circuits (e.g., III-V photonics, silicon photonics, and so on) [1–7], plasmonic waveguides [8–10], photonic crystal (PC) waveguides [14–21], topological photonic systems [22,23], etc. Even if advanced cladding or waveguide engineering techniques are applied [24–28], there is a limit in the minimal thickness of the cladding, beyond which the crosstalk between adjacent channels becomes enormously large. Here, we report an unprecedented strategy to construct ultracompact waveguide arrays without the cladding or wave-forbidden layers. Such unique waveguide systems are composed only of transmission channels with shifted spatial dispersions, which, simultaneously, function as the effective “cladding layers” of their adjacent channels. Therefore, the interchannel separation can be reduced to zero, bestowing the ultracompact zero-spacing waveguide arrays (ZSWAs). Based on low-loss all-dielectric PCs with shifted dispersions, we experimentally demonstrate the realization of such ZSWAs with negligible crosstalk. Furthermore, we find that such ZSWAs also exhibit the remarkable features of high-efficiency sharp bending and light routing to traverse the entire physical space. These findings break the traditional paradigm of waveguiding based on wave-forbidden cladding layers and pave a pathway toward ultracompact photonic circuits with extreme space utilization efficiency.

*Corresponding author.

rwpeng@nju.edu.cn

†Corresponding author.

muwang@nju.edu.cn

‡Corresponding author.

laiyun@nju.edu.cn

§T. S., H. C., and J. L. contributed equally to this work.

Published by the American Physical Society under the terms of the [Creative Commons Attribution 4.0 International license](https://creativecommons.org/licenses/by/4.0/). Further distribution of this work must maintain attribution to the author(s) and the published article's title, journal citation, and DOI.

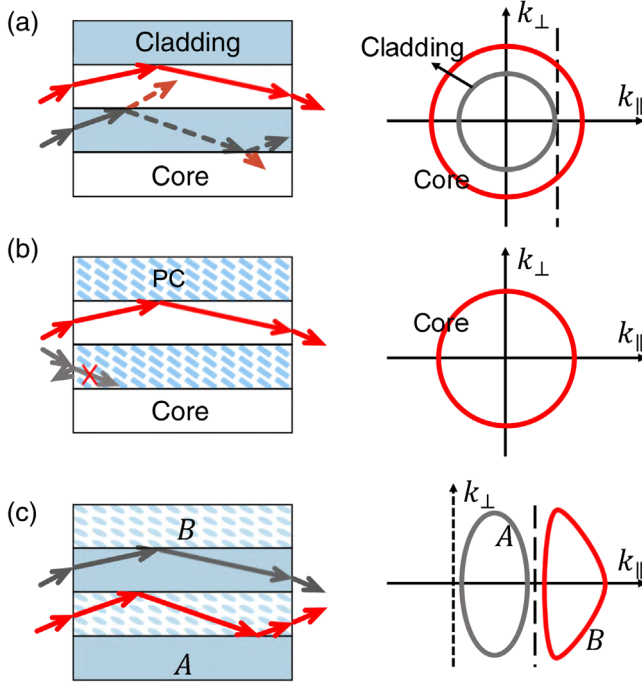


FIG. 1. Principles of traditional waveguide arrays and ZSWAs. The schematic diagrams of (a) traditional optical waveguides and (b) traditional PC waveguides that both require cladding layers and (c) ZSWAs with zero interchannel separation. The right panels demonstrate the equal frequency contours of the waveguide materials.

Figure 1 schematically demonstrates the fundamental difference between the traditional optical waveguide arrays, PC waveguide arrays, and the scheme of ZSWAs without cladding layers. The left panels show the schematics of transmission processes, and the right panels show the equal frequency contours (EFCs) of the materials comprising the waveguides. Here, k_{\parallel} and k_{\perp} denote the wave-vector components in the parallel and vertical directions of the waveguides, respectively. For waveguide modes, k_{\parallel} equals to the propagation constant β . In optical waveguide arrays [29], low-index cladding layers confine the waves inside the high-index core layers, as the $\beta(k_{\parallel})$ of the waveguide modes is larger than the wave number of the cladding layers (the dashed line). In PC waveguide arrays, waves can be confined in the core channels of an arbitrary index, e.g., free space, using the PCs with wave-forbidden photonic band gaps as the cladding layers. While in the scheme of ZSWAs, the system is solely composed of different transmission channels (denoted as A and B channels) with shifted spatial dispersions (or shifted EFCs), which is shown in Fig. 1(c). The EFCs of the materials in different channels are separated from each other in the direction of k_{\parallel} , and the propagating waves therein cannot be coupled. It immediately follows that all the channels can independently transmit waves despite the zero interchannel separation. On the other hand, if the EFCs of different channels

are not completely separated, the propagating waves could be coupled via abnormal refraction (see the Appendix A). Practically, there are some ways to realize such shifted spatial dispersion as required in Fig. 1(c). One approach is to construct effective gauge potentials [30–36], which have recently attracted a lot of attention. Here, we show that anisotropic all-dielectric PCs can also provide the required shifted dispersions [37,38], with the advantage of low loss and potential extension of optical bandwidth. We construct a proof-of-principle ZSWA system with two types of channels: the free space (air) and the PCs, respectively.

II. THEORY AND DESIGN OF THE ZSWA SYSTEM

For simplicity, two-dimensional PCs of transverse-magnetic (TM) polarization (electric field in the z axis) is considered. The symmetry of the PC plays an essential role in the design. In Fig. 2(a), we demonstrate the unit cells of two PCs with the group symmetries of C_4^v (I, square lattice and rods of $0.6a \times 0.6a$) and C_2^v (II, rectangular lattice and rods of $0.6a \times 0.4a$), respectively. Here, a is the lattice constant and $b = 0.6a$. The background is free space ($\epsilon_1 = 1$), and the dielectric rods have a permittivity $\epsilon_2 = 12$. The band structures of both PCs are calculated by the finite-element software COMSOL MULTIPHYSICS, as shown in Fig. 2(b), respectively. At a working frequency $fa/c = 0.2962$ [dashed line in Fig. 2(b)], the EFCs of the PCs I and II are shown as the gray and red lines in Figs. 2(c) and 2(d), respectively. The dotted box represents the boundary of the first Brillouin zone, and the black lines denote the circular EFCs of free space. Clearly, in PC I with the C_4^v symmetry, the band dispersions and EFCs are the same in the x and y directions, while the symmetry breaking from C_4^v to C_2^v in PC II removes this degeneracy, and more importantly, eliminates the elliptical EFC centered at the Y point. This symmetry breaking is a crucial step to open a partial band gap for ZSWAs. Since the elliptical EFC centered at the X point is shifted away from that of free space, the condition of separated spatial dispersions along the waveguiding direction in Fig. 1(c) is satisfied by PC II.

In addition to the shifted spatial dispersion, we also design the surface impedance of PC II to match that of free space on the y surface. In Fig. 2(e), we plot the calculated transmittance through N layers ($N = 6, 7, 8, 20$) of PC II in free space for different incident angles on the y surface at the working frequency. For all incident angles within $\pm 75^\circ$, the transmittance exceeds 95%, irrespective of the layer number N of the PC. This excellent impedance matching (see Appendix B) is also attributed to the PC structure [37,38], which can guarantee that the reflection on the port of the PC channel is negligibly small.

Next, we investigate two complementary types of waveguides, i.e., the PC channels in the free-space host and the free-space channels in the PC host, two primary components of the ZSWA. The schematic graphs are shown

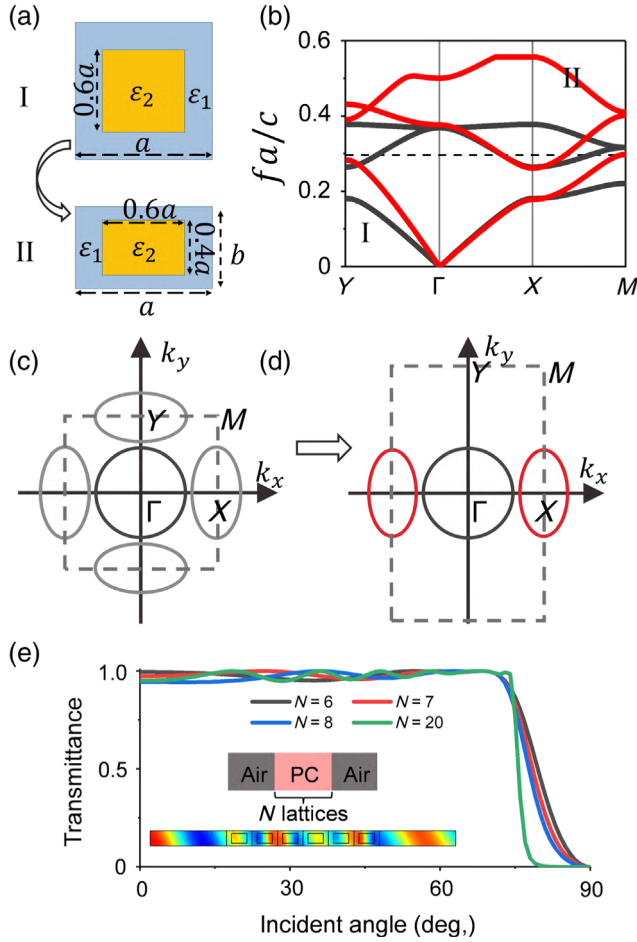


FIG. 2. The role of symmetry breaking in the PC design for shifted spatial dispersions. The unit cells (a), band structure for transverse-magnetic polarization (b), and equal frequency contours (c),(d) of two PCs I and II, which exhibit C_4^v and C_2^v symmetries, respectively. (e) The transmittance of the PC II with 6, 7, 8, and 20 layers. The insets show the simulation to calculate the transmittance.

in Figs. 3(a) and 3(b), respectively. In Figs. 3(c) and 3(e), we plot the band dispersions of the PC channels with $w = 4b$ and $w = 5b$, respectively, where w is the waveguide width. Clearly, the waveguide modes are all beyond the light cone (dashed line). At the working frequency (dotted line), one mode appears for the case of $w = 4b$ (even mode), and two modes appear for the case of $w = 5b$ (even and odd modes), as can be seen in the electric field distributions of the eigenmodes shown in inset graphs, respectively. On the other hand, Figs. 3(d) and 3(f) plot the band dispersions of the free-space channels with $w = 4b$ and $w = 5b$, respectively. At the working frequency, only one propagating mode (even mode) appears inside a partial band gap of the PC, which is within the light cone. Such a partial band gap directly results from the symmetry breaking from C_4^v to C_2^v . We emphasize that for both PC and free-space channels, propagating waveguide modes appear as long as the width $w \geq 2b$ (see Appendix C). When the

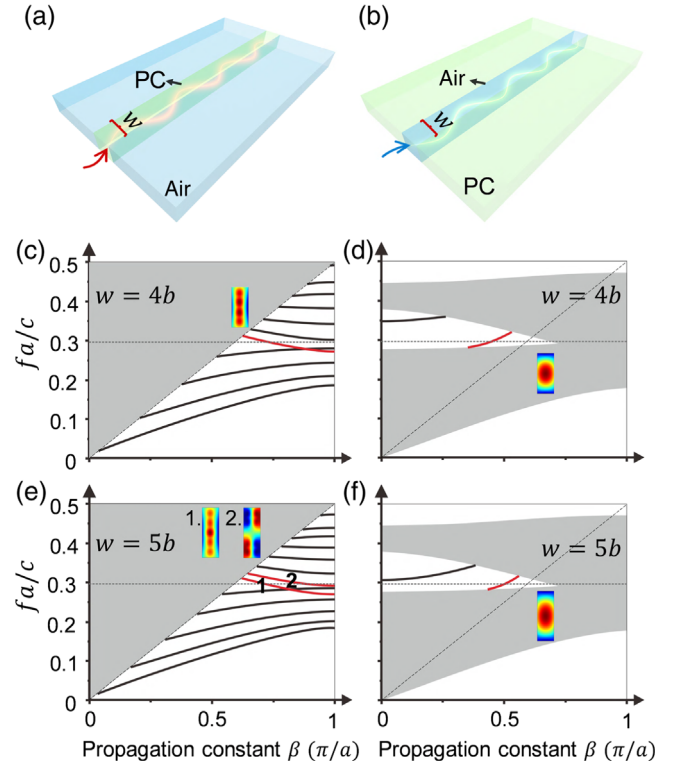


FIG. 3. Two complementary types of waveguides constructed by free space and PC II. (a),(b) The schematic diagrams of the PC channel (free-space cladding) and free-space channel (PC cladding), respectively. (c)–(f) The waveguide dispersions of the complementary PC and free-space channels with $w = 4b$ and $w = 5b$. The dashed line shows the light cone, and the dotted line marks the working frequency $fa/c = 0.2962$. The inset graphs show the electric field distributions of the corresponding waveguide modes.

width w further increases, the number of waveguide modes increases like the traditional optical waveguides. In addition, we find that the bandwidths of the waveguide modes are substantially large for optical communications.

III. SIMULATION AND EXPERIMENTAL RESULTS OF ZSWA CIRCUITS

By arranging the above PC II and free space alternately along the y direction, a ZSWA with zero interchannel separation is constructed, as shown in Fig. 4(a). Since the waveguide modes in the free-space and PC channels have $k_{\parallel} < k_0$ and $k_{\parallel} > k_0$, respectively, their crosstalk is inherently minimized. As a proof of principle, we experimentally fabricate this ZSWA at the microwave frequencies to demonstrate the zero-spacing transmission arrays, as shown in Fig. 4(b). The dielectric rods have $\epsilon = 12$, and the unit cell is of $a = 6$ mm and $b = 3.6$ mm. The working frequency is around 15 GHz. To demonstrate the arbitrariness of the width w , we design the waveguide array composed of four PC channels ($A_1/A_2/A_3/A_4$) and four

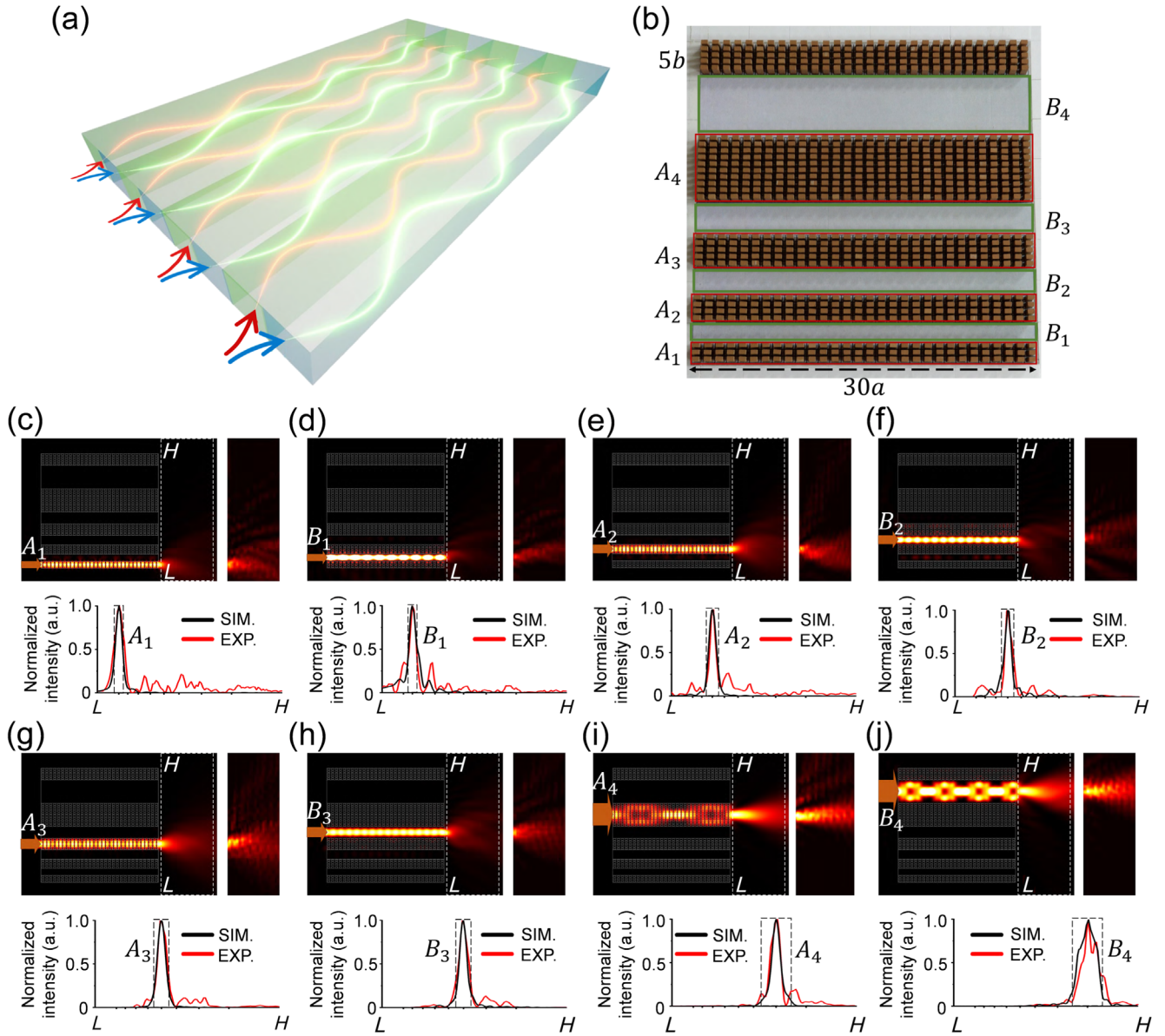


FIG. 4. Numerical and experimental demonstrations for ZSWAs. (a) Schematic graph of a ZSWA constructed by arranging PC and free-space channels alternately. (b) Photo of the experimental sample of the ZSWA. (c)–(j) The simulated (upper panel, left) and measured (upper panel, right) intensity patterns under the independent excitation of the eight channels (A_{1-4} , B_{1-4}). The white dashed frame marks the experimentally measured region. The lower panels show the normalized intensity distributions on the left edge of the measured region.

free-space channels ($B_1/B_2/B_3/B_4$) with different widths of $w = 3b/4b/5b/10b$, respectively. An additional PC layer with $w = 5b$ is placed beside the B_4 free-space channel to confine the waves. The electric field distributions of the propagating waveguide modes of the $A_2/B_2/A_3/B_3$ and $A_1/B_1/A_4/B_4$ channels are plotted in Fig. 3 and Appendix C, respectively.

We utilize a source for exciting the eight channels independently from their left ports. Using a two-dimensional microwave scanner (see Appendix D), we experimentally measure the intensity patterns for a region outside the right ports of the channels. In the upper panels

of Figs. 4(c)–4(j), we plot the simulated (left) and measured (right) intensity patterns of the ZSWA. The simulation results are obtained by COMSOL MULTIPHYSICS. The measurement is performed in the region with a small distance of 4 mm to the right ports, which is marked by the white dashed frame in Figs. 4(c)–4(j). The numerical and experimental results coincide well, confirming that wave transmission is well restricted within each channel when the channel is excited. From the independent transmission of waves through the eight channels (A_{1-4} , B_{1-4}), it is inferred that the crosstalk between the adjacent channels is negligible despite the zero interchannel separation. In a sense,

each type of channel acts simultaneously as the effective cladding layers for other channels. In the lower panels of Figs. 4(c)–4(j), we plot the normalized intensity distributions on the left edge of the measured region. For all cases, the peaks of the maximum intensities fall within the regions of the corresponding output ports (black dashed frames). In the experimental data, we also find that each channel has a bandwidth of around 13% when $w \geq 4b$, consistent with the theoretical prediction and simulation (see Appendix E).

We demonstrate that such ZSWAs possess the remarkable properties of sharp bending with negligible leakage and wave routing to traverse the entire physical space. In other words, ultracompact photonic circuits without cladding layers are realized. By orientating the PC II unit cell in the x or y direction, two types of channels that transmit waves only in the x or y direction can be realized, respectively. However, the free-space channel allows the transmission of waves in both the x and y directions. Next, we construct square-shaped supercells composed of $3a \times 5b$ units ($b = 0.6a$) of the PC or free space, as shown in Fig. 5(a). The red double-headed arrows denote the PC supercells, and the black cross arrows denote the free-space supercell. By appropriately arranging the three types of supercells, sharp bending and routing photonic circuits can be realized. A sample of the 90° sharp-bending array is illustrated in the left panel of Fig. 5(b), where three transmission channels with the input and output ports are denoted by I_i and O_i ($i = 1, 2, 3$), respectively. In Figs. 5(c)–5(e), we plot the intensity patterns for the three incidence cases from the input ports I_i ($i = 1, 2, 3$), respectively. The numerical results (left) and the corresponding experimental results (right) are plotted in the upper panels of Figs. 5(c)–5(e), respectively, which coincide well with each other. The experimental measurement is performed in the region marked by the white dashed frame. In the lower panels of Figs. 5(c)–5(e), we plot the normalized intensity distributions on the left edge of the measured region. In the cases of Figs. 5(d) and 5(e), the peaks of the maximum intensity fall within the regions of the output ports (black dashed frames). In the case of Fig. 5(c), the peak falls on the edge of the output port. This is induced by the excitation of the odd mode in the bent channel, as shown in Fig. 3(e). Here, we note that the mode conversion is avoidable by simple optimization of the free-space supercell, e.g., by adding two more dielectric cylinders (with $\epsilon = 12$) at two corners of the supercell (see Appendix F). The overall transmission efficiency of the 90° sharp bending can be improved to be around 93% and even higher. Despite the zero interchannel separation in this sharp-bending array, the leakage of waves is reasonably small, as shown in Figs. 5(c)–5(e).

A 180° bend can be realized via two successive 90° bends. In this case, a switch between the transmission in the free-space and PC channels is necessary. A photonic routing circuit can be constructed by applying a series

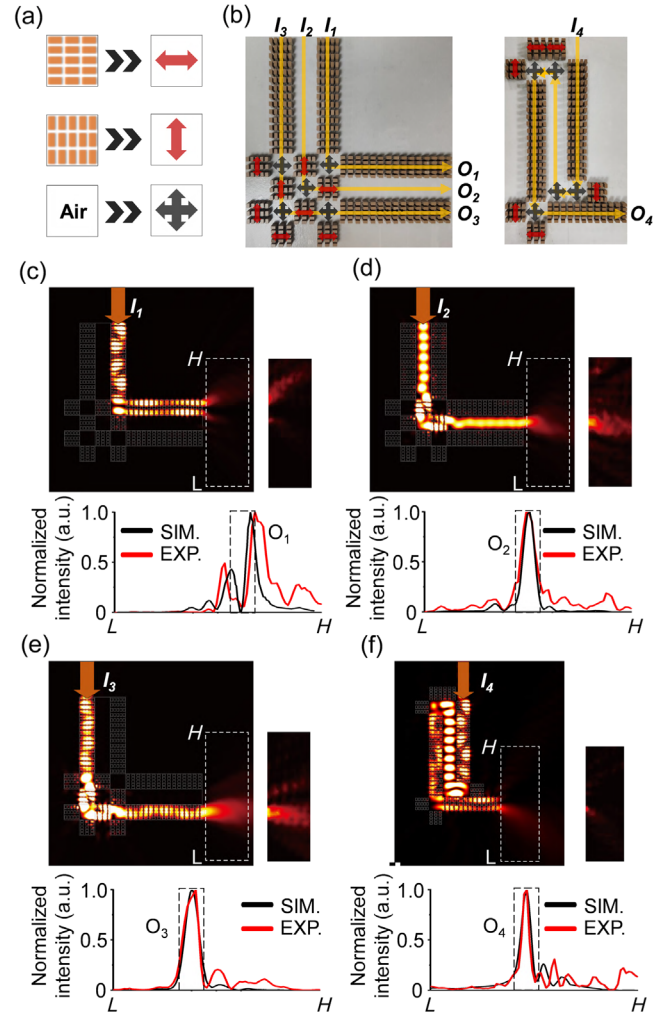


FIG. 5. Numerical and experimental demonstrations for sharp-bending and routing photonic circuits. (a) The PC or free-space supercells allow transmission in the x or y directions or both directions. (b) Left: photo of the experimental sample of the 90° bending arrays. There are three transmission paths from I_i to O_i ($i = 1, 2, 3$). Right: photo of the experimental sample of the routing circuit. The transmission path is from I_4 to O_4 . (c)–(f) The simulated (upper panel, left) and measured (upper panel, right) intensity patterns under independent excitation from the input ports I_i ($i = 1, 2, 3, 4$). The white dashed frame marks the experimentally measured regions. The lower panels show the normalized intensity distributions on the left edge of the measured region.

of the 90° and 180° bends, which can amazingly traverse the entire physical space. A sample of the photonic routing circuit is illustrated in the right panel of Fig. 5(b), which is composed of two 180° bends and one 90° bend. For incidence from the input port I_4 , waves will be routed to the output port O_4 . In the upper panel of Fig. 5(f), we plot the numerically calculated (left) and experimentally measured (right) intensity patterns, which coincide well with each other. The experimental measurement is performed in the region marked by the white dashed frame. In the

lower panel of Fig. 5(f), we plot the normalized intensity distributions on the left edge of the measured region, confirming the successful routing of waves. Through similar structural optimization of adding dielectric rods (with $\epsilon = 12$) in the free-space supercells at the bending part, the effect of backscattering in the 180° bend can be significantly suppressed, so that the overall transmittance is increased from 64% to 96% (see Appendix F). More complicated routing circuits such as the splitting (see Appendix G) can also be designed based on this principle.

The above demonstration is counterintuitive and intriguing as it is similar to realize a “labyrinth” (for photons) without using physical “walls” (cladding layers). This phenomenon is possible because photons are bestowed with different momenta via photonic structures. Such an intrinsic momentum difference removes the essential need for physical barriers, i.e., the wave-forbidden cladding layers, which are currently widely believed to be indispensable in waveguide systems.

In the following, we demonstrate an optical design of the ultracompact photonic circuits without cladding layers composed of silicon ($n = 3.48$) and silica ($n = 1.45$) [7]. The PC with shifted dispersion is a rectangular lattice of rectangular silicon rods ($0.7a \times 0.5a$) in a silica host, as plotted in the inset of Fig. 6(a). The lattice constants are $a = 370$ nm and $b = 0.75a$. The working wavelength is chosen as $\lambda = 1550$ nm, at which the loss is negligible. The EFCs of the PC and silica at the working frequency are plotted as the red and black lines in Fig. 6(a). Clearly, the condition of separated EFCs along the direction of propagation in Fig. 1(c) is well satisfied. We note that the designed PC is impedance matched with silica for all incident angles within $\pm 30^\circ$, as verified by the transmittance results for different thicknesses of the PCs [Fig. 6(b)]. This impedance matching condition could help increase the transmission efficiency at the ports and the bending parts of light routing circuits.

In Fig. 6(c), we plot the simulation results of one PC channel and one silica channel with no cladding between them. The width of the PC channel is $w_{\text{PC}} = 3b = 832.5$ nm. The width of the silica channel is $w_{\text{SiO}_2} = 600$ nm. Therefore, the separation between the central axes of two adjacent channels is $S = 716.25$ nm $< \lambda/2$. The length (propagating distance) of the two channels is set to be $1000 \mu\text{m}$ ($2703a$). The input and output ports are denoted by I_i and O_i ($i = 5, 6$), respectively. In Fig. 6(c), the simulated intensity patterns in the region near the output ports (940 – $980 \mu\text{m}$) are plotted under the independent excitation from the input ports I_i ($i = 5, 6$). Clearly, the waves are confined in the original channel after the propagation of $1000 \mu\text{m}$, indicating that there is no crosstalk despite the zero cladding. In fact, no matter how long the propagating distance is, the wave is strictly confined in the original channel due to the inherent mismatched momenta in the two channels. This scenario indicates that the coupling is precisely zero, which is clearly

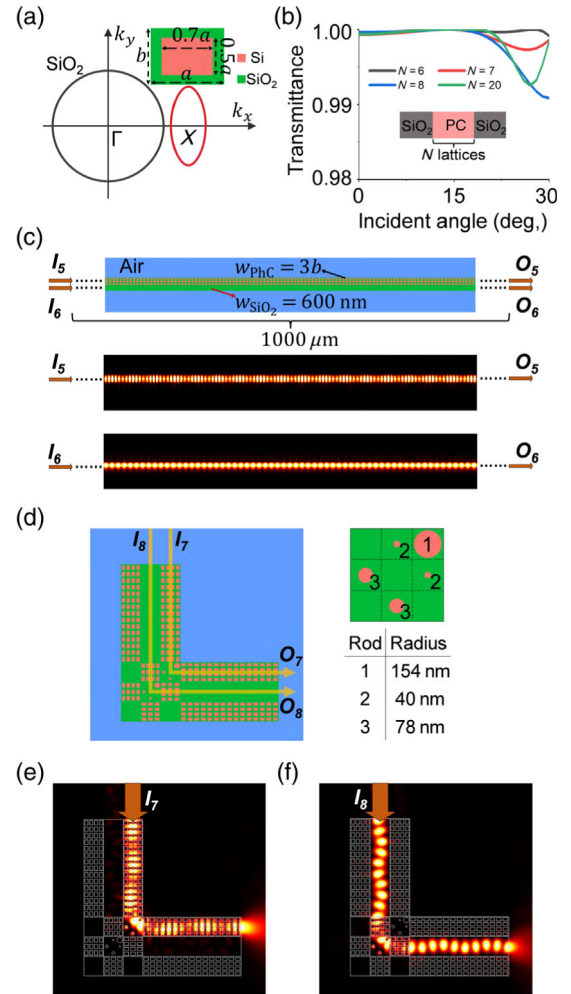


FIG. 6. Optical design of the ultracompact photonic circuits. (a) The unit cell and EFC of the PC. The lattice constant $a = 370$ nm and $b = 0.75a$. (b) The transmittance of the PC in silica with 6, 7, 8, and 20 layers. (c) The propagation of PC (I_5 – O_5) and silica channels (I_6 – O_6) with $1000 \mu\text{m}$ ($2703a$) propagating distance. The width of the PC (silica) channel is $w_{\text{PC}} = 3b = 832.5$ nm ($w_{\text{SiO}_2} = 600$ nm). (d) The schematic diagram of the PC (I_7 – O_7) and silica channels (I_8 – O_8) without any cladding between them. The right panels are the enlarged view of the corner supercells, and the table shows the radii of silicon rods. (e),(f) The simulated intensity distribution under independent excitation from the input ports I_i ($i = 7, 8$). The bending losses are -0.10 dB for the PC channel and -0.07 dB for the silica channel.

beyond the conventional waveguides. It is noteworthy that the waveguide structure is robust to the fabrication error and has a relatively large bandwidth from 1470 to 1600 nm (see Appendix H). Moreover, with the cladding removed, the separation between the central axes of two adjacent channels S is completely determined by the width of the transmission channels. Therefore, replacing the dielectrics with plasmonic or ultrahigh-refractive-index materials makes it possible to reduce S to the deep-subwavelength scale further.

Based on the PC design in Fig. 6(a), we also numerically demonstrate two 90° bending waveguides without

cladding. Such sharp-bending waveguides have zero bending radii R . The design is schematically shown in Fig. 6(d). Similar to Fig. 5(b), square supercells (side length $4b$) are utilized here. The input and output ports are denoted by I_i and O_i ($i = 7, 8$), respectively. In order to reduce the bending loss, structural optimization is performed at the corner of the bending waveguides by adding additional silicon rods. The enlarged view of the corner supercells and the radii of rods are shown in the right panel of Fig. 6(d). We note that this optimization process is similar to the method previously applied for bending waveguides made of line defects in PCs [20,21]. The simulated intensity patterns under independent excitation from the input ports I_i ($i = 7, 8$) are plotted in Figs. 6(e) and 6(f), respectively. Clearly, the propagation of waves is well confined in the original channel after the bending, which indicates negligible bending loss despite the zero cladding width and zero bending radius R . The overall transmittance is found to be 97.64% and 98.31% for the two bending channels I_7 - O_7 and I_8 - O_8 , which corresponds to the bending loss of -0.10 and -0.07 dB, respectively. This demonstration indicates that high-efficiency sharp-bending optical waveguides are possible and physically feasible without claddings.

IV. DISCUSSION AND CONCLUSIONS

The principle of constructing ZSWAs based on separated spatial dispersions is quite general and can be realized via various approaches, e.g., effective gauge potentials [30–36] or hyperbolic dispersions [39,40]. Here, we develop a PC approach based on pure dielectrics, and this approach is adaptive for many low-loss dielectric materials, including silicon, silicon nitride, and silicon dioxide. Therefore, our approach can be easily applied to optical or infrared frequencies based on the mature fabrication techniques in dielectric platforms. We note that previously a zero-index photonic chip consisting of silicon rods in a polymer matrix and clad by gold films has been experimentally demonstrated [41], which indicates the optical design in Fig. 6 is also feasible. This principle could be extended to more practical photonic chip systems such as SOI waveguides with further optimization.

Unlike previous endeavors that can shrink only the interchannel separation to a certain extent in the classical scheme of optical waveguides [24–28], our approach reduces the interchannel separation to exactly zero. Previously, several different methods have been proposed to reduce the interchannel separation, e.g., tuning the anisotropy of the cladding layer to make evanescent waves decay faster [24,25], tuning the geometric parameters (width) of the core layer to achieve exceptional coupling with extremely low crosstalk [26], or varying the thicknesses of the channels in a superlattice to obtain a more significant difference in propagation constant [27,28]. However, the minimum separation between the central axes of two adjacent channels S is still larger than $\lambda/2$, where λ is

the wavelength in free space. When the cladding thickness is further reduced, the coupling between the adjacent channels increases exponentially without exception. Here, by using shifted spatial dispersions beyond the classical scheme of optical waveguides, the thickness of cladding is reduced to zero for the first time. Intriguingly, our approach is complementary to the previously developed methods. The miniaturization can be further continued by reducing the width of the transmission channel, e.g., by using ultrahigh-refractive-index materials or plasmonic materials. In this sense, removing claddings is a giant leap toward the ultimate miniaturization of photonic waveguide systems.

The principle of ZSWAs is also fundamentally different from topological photonics [22,23]. Instead of using bulk modes, topological photonics utilizes edge modes that exist only on the interfaces between photonic-band-gap regions. Most of the space is occupied by photonic-band-gap regions, which are wave forbidden and cannot be utilized as transmission channels. The bulk-mode nature of ZSWAs provides excellent flexibility in the channel width (as shown in Fig. 4). Therefore, the advantages of both single-mode and multi-mode channels can be exploited easily for different purposes. Interestingly, high-efficiency sharp-bending ZSWA is also feasible by utilizing structure optimization [20,21]. These attractive features make the ZSWAs a potentially favorable platform for future photonic chips.

We note that in the experimental demonstrations the widths of the free-space and PC channels are large enough such that the coupling between the second-nearest-neighbor channels is negligibly small. In addition to increasing the channel widths, there are other ways to eliminate the crosstalk between the second-nearest-neighbor channels. One way is to engineer the anisotropy and geometric parameters of the structures to optimize the effective “cladding effect” to ensure near-zero coupling [24–26]. Another way is to introduce new channels whose spatial dispersions are apart from those of both the A and B channels, such that the new channels have no crosstalks with both the A and B channels in the system.

In conclusion, our work points out that the “common sense” in the traditional paradigm of waveguide physics, i.e., the necessity of the wave-forbidden cladding layers, is in fact a misunderstanding. We manage to transform such cladding layers into different transmission channels with no crosstalks by introducing the shifted spatial dispersions between their adjacent channels, leading to ZSWAs with unprecedented compactness and flexibility. This exciting discovery infers that there is actually no need for the physical “walls” (cladding layers) to build a “multilane” or a “labyrinth” for photons. The entire physical space can be composed of transmission channels, pushing the space utilization efficiency to the extreme level. This principle is universal for waves, and similar approaches can be applied to resolve the coupling issue of channels for microwaves, light, surface plasmons, etc.

ACKNOWLEDGMENTS

The authors acknowledge financial support from the National Key Research and Development Program of China (Grants No. 2020YFA0211300 and No. 2017YFA0303702) and the National Natural Science Foundation of China (Grants No. 12174188, No. 11974176, No. 11634005, No. 11974177, and No. 61975078).

APPENDIX A: ABNORMAL REFRACTION DUE TO THE OVERLAPPING EFCs

In Fig. 1, we discuss a waveguide array composed of A and B channels, where the wave is transmitted in both A and B channels. Such discussions are based on the assumption that the EFCs of A and B are completely separated from each other along the direction of propagation. In this Appendix, we discuss the abnormal refraction at the interface of A/B channels when the EFCs are not completely separated, as shown in Fig. 7(a). When the propagating constant $\beta(k_{\parallel})$ exceeds or falls behind the gray overlap region, the propagating mode is excited either in the B or A channels, respectively. In this case, the ZSWA still works. However, when $\beta(k_{\parallel})$ falls inside the overlapping gray region, the propagating modes of both A and B channels can be excited, which leads to the failure of the ZSWA.

Here we take a 1D PC $\varepsilon_1/\varepsilon_2/\varepsilon_1$ as medium A , and its structure is illustrated in Fig. 7(b). The relative permittivity and filling ratio of the material $\varepsilon_1/\varepsilon_2$ are $\varepsilon_1 = 2$ ($\varepsilon_2 = 6.5$) and 0.6 (0.4), respectively. When $fa/c = 0.4077$, the EFCs of this PC in the reduced Brillouin zone (dotted box) are shown in red lines in Fig. 7(c). Take free space as the medium B and its EFC are shown as the gray line in Fig. 7(c). For an incident wave with the wave vector denoted as a incident from free space onto the y - z surface of medium A , the eigenmodes with the wave vectors b and b' in PC and medium A could be excited due to the conservation of the wave-vector component along the y direction. Since waves do not travel backward, b is excited. When the wave hits the interface of medium A/B from medium A , the propagation mode with wave vector c in free space can be excited and negative refraction occurs. Figure 7(d) shows the numerical simulation of the electric field distribution of the Gaussian beam incident from the left free space (medium B) to medium A (size $80a \times 50a$) and then to the top free space (medium B) at an incidence angle of 40° . The theory and simulation match pretty well, indicating that when the EFCs of the materials or structures of the channels overlap each other along the propagation direction, abnormal refraction may emerge between the channels, leading to the destruction of the zero-spacing transmission array. To avoid this consequence, the EFCs should be completely separated from each other.

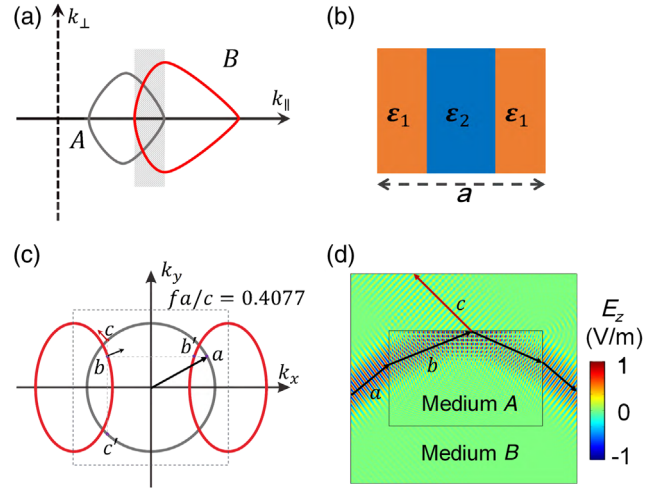


FIG. 7. Abnormal refraction due to the overlapping EFCs of medium A and B . (a) The schematic diagram of the EFCs of medium A and B when they have overlapping regions. (b) The structure of 1D PC with relative permittivity and filling ratio $\varepsilon_1 = 2$ ($\varepsilon_2 = 6.5$) and 0.6 (0.4). (c) The EFCs of medium A (1D PC) and B (free space) at the frequency $fa/c = 0.4077$. (d) Electric field distributions for a Gaussian beam incident onto the medium A (size $80a \times 50a$) under the incident angle of 40° . The background is medium B (free space).

APPENDIX B: NUMERICAL APERTURE AND COUPLING EFFICIENCY OF THE ZSWAs

The numerical aperture and coupling efficiency are the essential parameters for conventional waveguides. This Appendix investigates the numerical aperture and coupling efficiency of the ZSWAs presented in the main text.

Here we take the waveguide structures in Fig. 4 as an example. For the free-space channel or the PC channel, the all-angle total internal reflection always occurs at the interface of the free-space and PC channels due to the completely separated EFCs. Therefore, in the case of free-space background, numerical apertures of both channels (e.g., defined as $NA = \sin \alpha$ for multimode channels) can reach almost 1.

Another issue is the coupling efficiency which determines the wave energy transmitted into the waveguides from their ports. The free-space channels naturally have a high coupling efficiency in the free-space background. Next, we focus on the coupling efficiency between the designed PC and free space, which may be characterized by the surface impedance for different incident angles. Figure 8(a) shows the EFCs of the second band of the PC in Fig. 2, and the black curve is the EFC at the working frequency $fa/c = 0.2962$. By matching the wave impedance of the PC with that of free space, we first calculate the impedance of free space $Z_{\text{air}} = -\omega\mu_0/\sqrt{k_0^2 - k_y^2}$. The wave impedance of the PC can be retrieved from the fields of the eigenstates as $Z_{\text{PC}} = \langle E_Z^{\text{PC}} \rangle_{yz} / \langle H_Y^{\text{PC}} \rangle_{yz}$, where $\langle E_Z^{\text{PC}} \rangle_{yz}$ (or

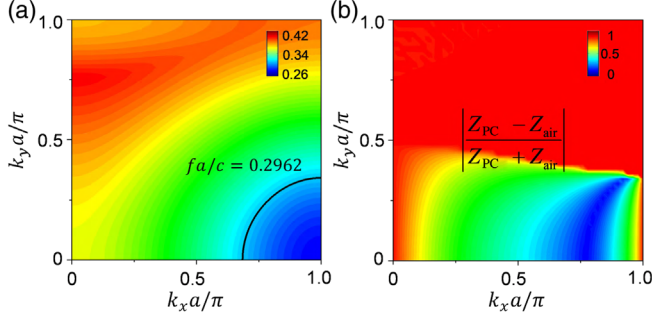


FIG. 8. Impedance matching between photonic crystal and air. (a) The EFCs of the second band of the PC II in Fig. 2. The black curve is the EFC at the working frequency $fa/c = 0.2962$. (b) The impedance difference between the PC and air of the second band.

$\langle H_y^{\text{PC}} \rangle_{yz}$) represents the average of the z component of electric field (or the y component of magnetic field) on the y - z surface for an eigenstate. Figure 8(b) shows the impedance difference $|(Z_{\text{PC}} - Z_{\text{air}})/(Z_{\text{PC}} + Z_{\text{air}})|$ of the PC and free space of the second band. It can be seen that at the frequency $fa/c = 0.2962$, the impedances of the PC and free space are almost the same, which proves that the PC channel can also have a high coupling efficiency with free space. This is further verified by the transmission investigation for different incident angles in Fig. 2(e).

APPENDIX C: WAVEGUIDE MODES OF PC AND FREE-SPACE CHANNELS

Different waveguide modes exist for different waveguide widths. Figure 4 shows an eight-channel ZSWA, and the waveguide modes of the $A_2/B_2/A_3/B_3$ channels are plotted in Fig. 3. In the following, we plot more waveguide modes for PC and free-space channels of different widths, and the A_1/B_1 and A_4/B_4 channels are also included.

In Figs. 9(a), 9(c), and 9(e), we plot the band dispersions of the waveguide modes confined in the PC channel with $w = 2b$, $w = 3b$, and $w = 10b$, respectively. The gray region is the light cone, and the black and red lines are the dispersion curves of the PC channels. Similarly, Figs. 9(b), 9(d), and 9(f) plot the band dispersions of the waveguide modes confined in the free-space channel with $w = 2b$, $w = 3b$, and $w = 10b$. Here the gray region is the PC band structure, and the black and red lines are the dispersion curves of the free-space channel. It is observed that the guided modes exist in both PC and free-space channels with different channel widths. Taken $fa/c = 0.2962$ as the working frequency, the electric field distributions of the waveguide modes are plotted in the inset graphs.

Obviously, for both PC and free-space channels, guided modes exist for any channel width $w \geq 2b$, and the mode number increases with the width of the channels.

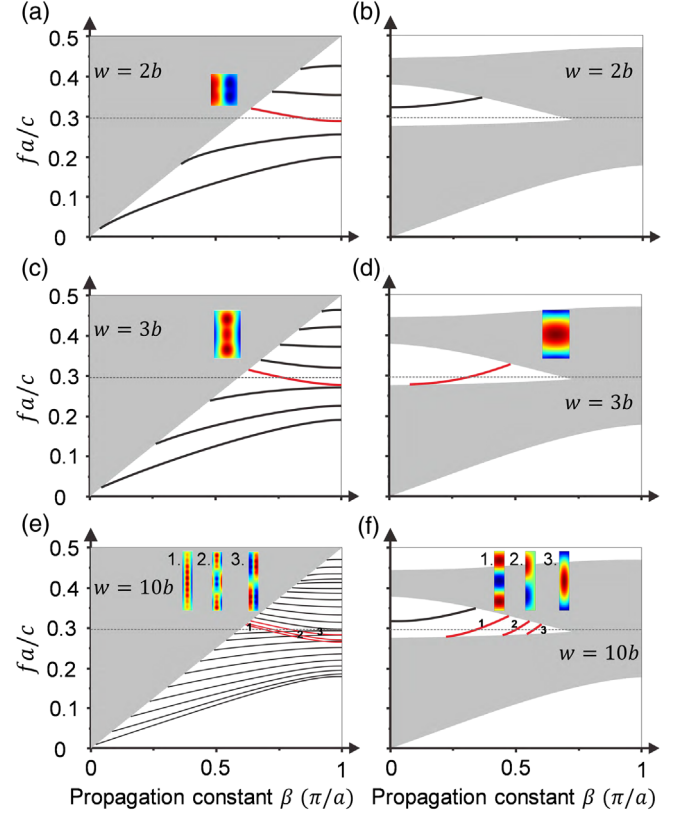


FIG. 9. Field distributions of the waveguide modes of the PC or free-space channels. (a) The waveguide mode of a PC channel with $w = 2b$. (b) The waveguide mode of an air channel with $w = 2b$. (c) The waveguide mode of a PC channel with $w = 3b$. (d) The waveguide mode of an air channel with $w = 3b$. (e) The waveguide mode of a PC channel with $w = 10b$. (f) The waveguide mode of an air channel with $w = 10b$. The red line indicates their modes at working frequency $fa/c = 0.2962$ (dashed line), and the illustrations show the electric field distribution of these propagation modes. The gray region shows the free-space (PC) band structure, and the black and red lines are the dispersion curves of the PC (free-space) channel.

APPENDIX D: METHODS OF SIMULATION AND EXPERIMENT

1. Simulation

The simulation results are obtained from the finite-element commercial solver COMSOL MULTIPHYSICS 5.5. The EFCs and band structure of PCs are calculated using a continuum Floquet eigensolver with Floquet periodic boundary conditions in the two lattice vector directions. The transmittances are retrieved from S parameters of ports and have Floquet periodic boundary conditions in the direction perpendicular to the wave vector to ensure slabs. The full-wave simulations are obtained from ports in the frequency domain.

2. Experimental setup

In the microwave experiments, the fabricated PC consisting of alumina ceramic rods is assembled inside a

parallel-plate waveguide composed of two flat aluminum plates. The separation between the two aluminum plates is 8 mm, which equals the height of the PC. The separation is less than half of the wavelength of interest (i.e., 20 mm for 15 GHz) to ensure that the parallel-plate waveguide supports only transverse electromagnetic modes. A standard Ku-band waveguide accompanied with absorbing materials generates a beam with a finite width. The electric field is measured via a probing antenna inside the parallel-plate waveguide. This probing antenna is mounted by a stepper motor. The emitting Ku-band waveguide and the probing antenna are connected to a KEYSIGHT N5224B network analyzer to acquire both the magnitude and phase of the microwave signal at the position of the probing antenna.

APPENDIX E: BANDWIDTH ANALYSIS OF PC AND FREE-SPACE CHANNELS

In this Appendix, we analyze the bandwidth of the eight channels in Fig. 4 from the perspectives of theory, simulation, and experiment. By calculating the band dispersions of the waveguide modes in Figs. 3 and 9, the theoretical bandwidth of each waveguide channel can be obtained. Here we define the frequency range covered by the dispersion of the waveguide mode as the bandwidth of each channel. When several waveguide modes overlap in frequency, the bandwidth is the union of the frequencies of these modes. In simulations and experiments, the ZSWA is considered valid when the transmitted wave intensity is concentrated at the corresponding outports of the channel. Based on this criterion, we obtain the bandwidth of each channel. Table I shows the bandwidths achieved by the theoretical band structure, simulation, and experimental results for the eight channels in Fig. 4. It can be seen that when $w \geq 4b$, each channel has a bandwidth greater than 13%, and the bandwidths achieved from the theory, simulation, and experiment are consistent with each other.

TABLE I. The bandwidth of the waveguide array. In theory, when several waveguide modes overlap in frequency, the bandwidth is the union of the frequencies of these modes.

Channel	Theory (GHz)	SIM. (GHz)	EXP. (GHz)
A1	14–15.7	14.3–15.9	15.2–16.4
B1	14.3–16.3	14.4–16.4	15.2–16.8
A2	13.7–16.4 (2 modes)	13.9–15.9	14.3–16.0
B2	14.3–15.9	14.2–15.9	14.4–15.9
A3	13.5–17.0 (3 modes)	13.7–16.8	13.9–16.9
B3	14.5–17.1 (2 modes)	14.4–17.0	14.9–16.9
A4	13.3–17.4 (6 modes)	13.5–17.0	13.6–16.9
B4	14.1–17.4 (4 modes)	14.1–17.3	14.1–17.7

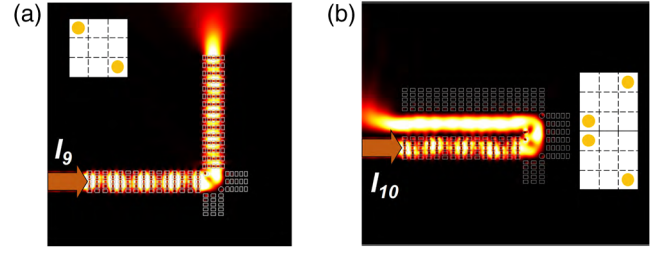


FIG. 10. Structural optimization in corner supercells to improve the transmission efficiency in bending circuits. (a),(b) The simulated intensity distributions under independent excitation from the input ports I_9 and I_{10} . The insets are the enlarged views of the structure at the corner supercells. These yellow rods have radius $r = 2$ mm and permittivity $\epsilon = 12$. The other parameters are the same as in Figs. 4 and 5. The transmission efficiency of 90° bend (a) increases from 83% to 93%, and the transmission efficiency of 180° bend (b) increases from 64% to 96%.

APPENDIX F: IMPROVE THE TRANSMISSION EFFICIENCY IN BENDING CIRCUITS

The bending loss is induced by the coupling loss at the corner supercells of ZSWAs. In addition, the mode conversion introduces extra bending loss, too. This Appendix discusses how to improve the transmission efficiency of bending circuits and suppress the mode conversion in Fig. 5(c).

In Fig. 10(a), two dielectric rods with $\epsilon = 12$ are placed in the corner supercells to suppress the mode conversion. The total transmission efficiency is defined by P_{IP}/P_{OP} , where P_{IP} is the input power, and P_{OP} is the power at the output of each bending circuit. It is seen that unlike the case of mode conversion in Fig. 5(c), it is still an even mode after 90° bending, and the total transmission efficiency has increased from 83% to 93%. Moreover, at the first 180° bend in Fig. 5(f), the transmission efficiency is only 64%, which is mainly caused by backscattering. In order to eliminate the backscattering, four dielectric rods with $\epsilon = 12$ are added in the two corner supercells in Fig. 10(b). Successfully, the total transmission efficiency increases from 64% to 96%. It is expected that the transmission efficiency of the bending circuit can be further improved by structural optimization.

APPENDIX G: SPLITTING PHOTONIC CIRCUIT DESIGNS

We introduce three kinds of corner supercells (two PC supercells and one free-space supercell) in Fig. 5(a) to realize the bending of ZSWAs. Intriguingly, by arranging these basic supercells, we can easily design two types of splitting photonic circuits with zero interchannel separation, as shown in Fig. 11.

In Fig. 11(a), we demonstrate a splitting photonic circuit. Unlike traditional beam splitters, it has one input and three output ports, and the three output ports have zero

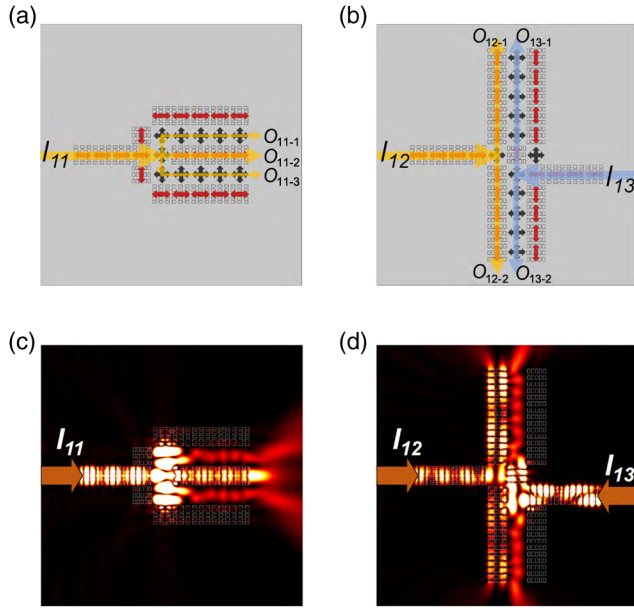


FIG. 11. Splitting photonic circuit designs with zero-spacing distance. (a) A splitting photonic circuit has one input port and three output ports with zero interchannel separation. (b) The splitting photonic circuit has two input ports and four output ports with zero interchannel separation. (c),(d) The simulated intensity distributions under independent excitation from the input ports I_i ($i = 11, 12, 13$).

interchannel separation. Moreover, in Fig. 11(b), we introduce another splitting photonic circuit that has two input ports and four output ports, and there is no interchannel separation between the four outputs. The simulated intensity distribution under independent excitation of the input ports I_i ($i = 11, 12, 13$) are plotted in Figs. 11(c) and 11(d). These results show that both splitting photonic circuits work well even though there is no interchannel separation between output channels.

APPENDIX H: THE FABRICATION TOLERANCE AND BANDWIDTH OF THE OPTICAL WAVEGUIDE STRUCTURE

This Appendix demonstrates that the optical waveguide structure has a significant fabrication tolerance and a broad bandwidth. The PC in Fig. 6 is a rectangular lattice of rectangular silicon rods in a silica host. The length and width of the rectangular silicon rod are $0.7a$ and $0.5a$, respectively. In the following, we demonstrate that both length l_1 and width l_2 [as shown in Fig. 12(a)] have a large fabrication tolerance.

We fix the width of the PC and silica channels to be 832.5 and 600 nm, respectively, which is the same as those in Fig. 6(c). The length (propagation distance) of the two channels is set as $1000 \mu\text{m}$ ($2703a$). The input and output ports are denoted by I_i and O_i ($i = 5, 6$), respectively. If we fix the width of the silicon rod as $l_2 = 0.5a$, the waveguide

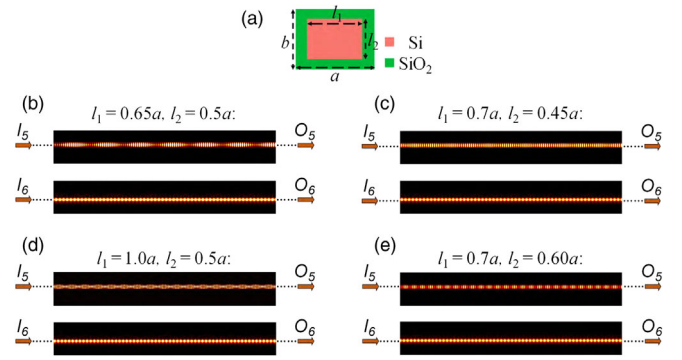


FIG. 12. The fabrication tolerance of the waveguide structure in Fig. 6. (a) The unit cell of PC channel with two variables l_1 and l_2 . (b)–(e) The simulated intensity patterns in the region near the output ports ($940\text{--}980 \mu\text{m}$) with the sizes of silicon rods $l_1 = 0.65a$, $l_2 = 0.5a$ (b), $l_1 = 0.7a$, $l_2 = 0.45a$ (c), $l_1 = 1.0a$, $l_2 = 0.5a$ (d), and $l_1 = 0.7a$, $l_2 = 0.60a$ (e). The propagation length of PC ($I_5\text{--}O_5$) and silica channels ($I_6\text{--}O_6$) is $1000 \mu\text{m}$ ($2703a$) and the working wavelength is 1550 nm. The width of the PC (silica) channel is 832.5 nm (600 nm).

system still works when the length of silicon rod l_1 varies from $0.65a$ to $1.0a$ at the working wavelength of 1550 nm. Specifically, the simulated intensity patterns in the region near the output ports ($940\text{--}980 \mu\text{m}$) are plotted in Figs. 12(b) and 12(d) with the lengths of silicon rods l_1 equal to $0.65a$ and $1.0a$, respectively. Clearly, the waves are confined in the original channel after the propagation of $1000 \mu\text{m}$, indicating no crosstalk despite the significant difference in l_1 . Similarly, when l_1 is fixed as $0.7a$, the waveguide system still works with l_2 varying from $0.45a$ to $0.60a$, as shown in Figs. 12(c) and 12(e). In conclusion, the waveguide structure is relatively robust to fabrication error.

Regarding the bandwidth, we note that the principle presented here is theoretically applicable to an extended

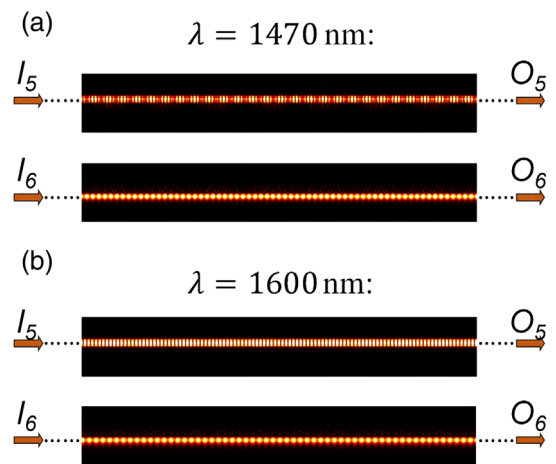


FIG. 13. The bandwidth of the optical waveguide structure. (a), (b) The simulated intensity patterns in the region near the output ports ($940\text{--}980 \mu\text{m}$) with wavelength $\lambda = 1470$ and 1600 nm. All geometric parameters are the same as those in Fig. 6.

frequency because the shifted spatial dispersion occurs in a relatively broad frequency range, as shown in Fig. 3. By investigating the waveguide structure in Fig. 6, we find that the waveguide structure at least has a bandwidth ranging from 1470 to 1600 nm, which is sufficient for most optical chips. Figures 13(a) and 13(b) plot the simulated intensity patterns in the region near the output ports (940–980 μm) with wavelength $\lambda = 1470$ and 1600 nm, respectively. These results confirm that the waveguide structure has a broad bandwidth with low-propagation losses.

-
- [1] G. T. Reed, *The Optical Age of Silicon*, *Nature (London)* **427**, 595 (2004).
- [2] M. Lipson, *Guiding, Modulating, and Emitting Light on Silicon—Challenges and Opportunities*, *J. Lightwave Technol.* **23**, 4222 (2005).
- [3] D. Dai, J. Bauters, and J. E. Bowers, *Passive Technologies for Future Large-Scale Photonic Integrated Circuits on Silicon: Polarization Handling, Light Non-Reciprocity and Loss Reduction*, *Light Sci. Appl.* **1**, e1 (2012).
- [4] D. Dai, L. Liu, S. Gao, D.-X. Xu, and S. He, *Polarization Management for Silicon Photonic Integrated Circuits*, *Laser Photonics Rev.* **7**, 303 (2013).
- [5] S. Pathak, in *Nanoelectronics*, edited by B. K. Kaushik (Elsevier, New York, 2019), p. 219.
- [6] M. Smit, K. Williams, and J. v. d. Tol, *Past, Present, and Future of InP-Based Photonic Integration*, *APL Photonics* **4**, 050901 (2019).
- [7] Y. Liu *et al.*, *Arbitrarily Routed Mode-Division Multiplexed Photonic Circuits for Dense Integration*, *Nat. Commun.* **10**, 3263 (2019).
- [8] E. N. Economou, *Surface Plasmons in Thin Films*, *Phys. Rev.* **182**, 539 (1969).
- [9] S. I. Bozhevolnyi, V. S. Volkov, E. Devaux, and T. W. Ebbesen, *Channel Plasmon-Polariton Guiding by Subwavelength Metal Grooves*, *Phys. Rev. Lett.* **95**, 046802 (2005).
- [10] Y. Fang and M. Sun, *Nanoplasmonic Waveguides: Towards Applications in Integrated Nanophotonic Circuits*, *Light Sci. Appl.* **4**, e294 (2015).
- [11] R. Katouf, N. Yamamoto, A. Kanno, N. Sekine, K. Akahane, H. Sotobayashi, T. Isu, and M. Tsuchiya, *Ultra-high Relative Refractive Index Contrast GaAs Nanowire Waveguides*, *Appl. Phys. Express* **1** (2008).
- [12] Y. He, S. He, J. Gao, and X. Yang, *Nanoscale Metamaterial Optical Waveguides with Ultrahigh Refractive Indices*, *J. Opt. Soc. Am. B* **29**, 2559 (2012).
- [13] N. Marcuvitz, *Waveguide Handbook* (McGraw-Hill, New York, NY, 1951).
- [14] E. Yablonovitch, *Inhibited Spontaneous Emission in Solid-State Physics and Electronics*, *Phys. Rev. Lett.* **58**, 2059 (1987).
- [15] S.-Y. Lin, E. Chow, V. Hietala, P. R. Villeneuve, and J. D. Joannopoulos, *Experimental Demonstration of Guiding and Bending of Electromagnetic Waves in a Photonic Crystal*, *Science* **282**, 274 (1998).
- [16] S. John, *Strong Localization of Photons in Certain Disordered Dielectric Superlattices*, *Phys. Rev. Lett.* **58**, 2486 (1987).
- [17] J. D. Joannopoulos, S. G. Johnson, J. N. Winn, and R. D. Meade, *Photonic Crystals: Molding the Flow of Light*, 2nd ed. (Princeton University Press, Princeton, NJ, 2011).
- [18] D. N. Christodoulides, F. Lederer, and Y. Silberberg, *Discretizing Light Behaviour in Linear and Nonlinear Waveguide Lattices*, *Nature (London)* **424**, 817 (2003).
- [19] P. Russell, *Photonic Crystal Fibers*, *Science* **299**, 358 (2003).
- [20] A. Mekis, J. C. Chen, I. Kurland, S. Fan, P. R. Villeneuve, and J. D. Joannopoulos, *High Transmission through Sharp Bends in Photonic Crystal Waveguides*, *Phys. Rev. Lett.* **77**, 3787 (1996).
- [21] V. Liu and S. Fan, *Compact Bends for Multi-Mode Photonic Crystal Waveguides with High Transmission and Suppressed Modal Crosstalk*, *Opt. Express* **21**, 8069 (2013).
- [22] A. B. Khanikaev and G. Shvets, *Two-Dimensional Topological Photonics*, *Nat. Photonics* **11**, 763 (2017).
- [23] L. Lu, J. D. Joannopoulos, and M. Soljačić, *Topological Photonics*, *Nat. Photonics* **8**, 821 (2014).
- [24] S. Jahani and Z. Jacob, *Transparent Subdiffraction Optics: Nanoscale Light Confinement without Metal*, *Optica* **1**, 96 (2014).
- [25] S. Jahani *et al.*, *Controlling Evanescent Waves Using Silicon Photonic All-Dielectric Metamaterials for Dense Integration*, *Nat. Commun.* **9**, 1893 (2018).
- [26] M. B. Mia, S. Z. Ahmed, I. Ahmed, Y. J. Lee, M. Qi, and S. Kim, *Exceptional Coupling in Photonic Anisotropic Metamaterials for Extremely Low Waveguide Crosstalk*, *Optica* **7**, 881 (2020).
- [27] W. Song, R. Gatlula, S. Abbaslou, M. Lu, A. Stein, W. Y.-C. Lai, J. Provine, R. F. W. Pease, D. N. Christodoulides, and W. Jiang, *High-Density Waveguide Superlattices with Low Crosstalk*, *Nat. Commun.* **6**, 7027 (2015).
- [28] R. Gatlula, S. Abbaslou, M. Lu, A. Stein, and W. Jiang, *Guiding Light in Bent Waveguide Superlattices with Low Crosstalk*, *Optica* **6**, 585 (2019).
- [29] K. Okamoto, *Fundamentals of Optical Waveguides* (Academic, San Diego, 2006).
- [30] K. Fang and S. Fan, *Controlling the Flow of Light Using the Inhomogeneous Effective Gauge Field that Emerges from Dynamic Modulation*, *Phys. Rev. Lett.* **111**, 203901 (2013).
- [31] F. Liu, T. Xu, S. Wang, Z. H. Hang, and J. Li, *Polarization Beam Splitting with Gauge Field Metamaterials*, *Adv. Opt. Mater.* **7**, 1801582 (2019).
- [32] Y. Chen, R.-Y. Zhang, Z. Xiong, Z. H. Hang, J. Li, J. Q. Shen, and C. T. Chan, *Non-Abelian Gauge Field Optics*, *Nat. Commun.* **10**, 3125 (2019).
- [33] Y. Lumer, M. A. Bandres, M. Heinrich, L. J. Maczewsky, H. Herzig-Sheinfux, A. Szameit, and M. Segev, *Light Guiding by Artificial Gauge Fields*, *Nat. Photonics* **13**, 339 (2019).
- [34] W.-J. Chen, B. Hou, Z.-Q. Zhang, J. B. Pendry, and C. T. Chan, *Metamaterials with Index Ellipsoids at Arbitrary k -Points*, *Nat. Commun.* **9**, 2086 (2018).
- [35] F. Liu and J. Li, *Gauge Field Optics with Anisotropic Media*, *Phys. Rev. Lett.* **114**, 103902 (2015).
- [36] Q. Lin and S. Fan, *Light Guiding by Effective Gauge Field for Photons*, *Phys. Rev. X* **4**, 031031 (2014).
- [37] J. Luo, Y. Yang, Z. Yao, W. Lu, B. Hou, Z. H. Hang, C. T. Chan, and Y. Lai, *Ultrasensitive Media and Transformation Optics with Shifted Spatial Dispersions*, *Phys. Rev. Lett.* **117**, 223901 (2016).

- [38] S. Li, Y. Wang, W. Zhang, W. Lu, B. Hou, J. Luo, and Y. Lai, *Observation of Wide-Angle Impedance Matching in Terahertz Photonic Crystals*, *New J. Phys.* **22**, 023033 (2020).
- [39] A. Poddubny, I. Iorsh, P. Belov, and Y. Kivshar, *Hyperbolic Metamaterials*, *Nat. Photonics* **7**, 948 (2013).
- [40] V. E. Babicheva, M. Y. Shalaginov, S. Ishii, A. Boltasseva, and A. V. Kildishev, *Finite-Width Plasmonic Waveguides with Hyperbolic Multilayer Cladding*, *Opt. Express* **23**, 9681 (2015).
- [41] Y. Li, S. Kita, P. Muñoz, O. Reshef, D. I. Vulis, M. Yin, M. Lončar, and E. Mazur, *On-Chip Zero-Index Metamaterials*, *Nat. Photonics* **9**, 738 (2015).